

## TESTING X-RAY MEASUREMENTS OF GALAXY CLUSTERS WITH COSMOLOGICAL SIMULATIONS

DAISUKE NAGAI<sup>1</sup>, ALEXEY VIKHLININ<sup>2,3</sup>, ANDREY V. KRAVTSOV<sup>4</sup>

*The Astrophysical Journal, submitted*

### ABSTRACT

X-ray observations of galaxy clusters potentially provide powerful cosmological probes if systematics due to our incomplete knowledge of the intracluster medium (ICM) physics are understood and controlled. In this paper, we present mock *Chandra* analyses of cosmological cluster simulations and assess X-ray measurements of galaxy cluster properties using a model and procedure essentially identical to that used in real data analysis. We show that reconstruction of three-dimensional ICM density and temperature profiles is excellent for relaxed clusters, but still reasonably accurate for unrelaxed systems. The total ICM mass is measured quite accurately ( $\lesssim 6\%$ ) in all clusters, while the hydrostatic estimate of the gravitationally bound mass is biased low by about 5%–20% through the virial region, primarily due to additional pressure support provided by subsonic bulk motions in the ICM, ubiquitous in our simulations even in relaxed systems. Gas fraction determinations are therefore biased high; the bias increases toward cluster outskirts and depends sensitively on its dynamical state, but we do not observe significant trends of the bias with cluster mass or redshift. We also find that different average ICM temperatures, such as the X-ray spectroscopic  $T_{\text{spec}}$  and gas-mass-weighted  $T_{\text{mg}}$ , are related to each other by a constant factor with a relatively small object-to-object scatter and no systematic trend with mass, redshift or the dynamical state of clusters. We briefly discuss direct applications of our results for different cluster-based cosmological tests.

*Subject headings:* cosmology: theory—clusters: formation— methods: numerical

### 1. INTRODUCTION

X-ray observations of clusters of galaxies can potentially provide plethora of useful cosmological information. The cluster-based cosmological tests include cluster number counts based on the temperature function, baryon fraction and X-ray and SZ Hubble constant measurements. These cosmological tests provide potentially very powerful constraints on the matter density,  $\Omega_M$ ,  $\Omega_\Lambda$ ,  $\sigma_8$ , and the equation of state of dark energy,  $w$ . In all of these cosmological tests, the key observational ingredients are the gas mass ( $M_{\text{gas}}$ ), total mass ( $M_{\text{tot}}$ ), gas mass fractions ( $f_{\text{gas}} \equiv M_{\text{gas}}/M_{\text{tot}}$ ), and average cluster temperature ( $\langle T \rangle$ ). In the era of precision cosmology, it is paramount to achieve accurate measurements of the key cluster parameters, check how they depend on various simplifying assumptions, and control systematics due to our incomplete knowledge of the ICM physics.

There are many important simplifying assumptions used in deriving cluster properties from X-ray data. For example, it is usually assumed that the ICM density is a function of radius only and does not have small-scale substructure. However, substructure in clusters is ubiquitous and this biases the X-ray derived  $M_{\text{gas}}$  high (Mathiesen et al. 1999). Also, the small-scale clumps are often associated with subhalos and thus have lower temperature. Neglecting this can bias the average spectroscopic temperature of the cluster as a whole (Mathiesen & Evrard 2001; Mazzotta et al. 2004) which could potentially lead to biases in constraints on cosmological parameters (Rasia et al. 2005). Cluster total masses are often esti-

mated assuming the hydrostatic equilibrium for the ICM. This may underestimate the true gravitational bound mass if non-thermal pressure support is present. For example, turbulent gas motions can provide about 10%–20% of the total pressure support even in relaxed clusters and hence bias the hydrostatic estimate (Schuecker et al. 2004; Faltenbacher et al. 2005; Rasia et al. 2006; Lau et al. 2006). Spherical symmetry is another commonly used assumption useful in solving for three-dimensional (3D) physical cluster properties from two-dimensional (2D) observed quantities, but could bias results if clusters are aspherical.

X-ray observations with *Chandra* and *XMM-Newton* enable us to study properties of the ICM with unprecedented detail and accuracy and provide important handles on the ICM modeling and associated systematics. Their superb spatial resolution and sensitivity enable accurate X-ray brightness and temperature measurements at a large fraction of the cluster virial radius and also make it simple to detect most of the small-scale X-ray clumps. Despite this recent observational progress, the biases in the determination of the key cluster properties remain relatively uncertain. The main obstacle is that because of their unrivaled statistical accuracy, the X-ray results cannot be contrasted against any other independent observational techniques. In this study, we attempt to check the validity of the X-ray analyses, with a specific focus on the analyses of high-resolution *Chandra* data, by using mock observations of clusters derived from cosmological simulations, for which the true answers are known.

Our simulations properly treat both collisionless dynamics of dark matter and stars and gasdynamics and capture a variety of physical phenomena from the nonlinear collapse and merging of dark matter to shock-heating and radiative cooling of gas, star formation, chemical enrichment of the ICM by supernova and energy feedback. These simulations can therefore be used to test observational biases due to incomplete relaxation of gas, the dynamical state of a cluster, substructure, or non-isothermality. As we show in the forthcoming papers,

<sup>1</sup> Theoretical Astrophysics, California Institute of Technology, Mail Code 130-33, Pasadena, CA 91125 (daisuke@caltech.edu)

<sup>2</sup> Harvard-Smithsonian Center for Astrophysics, 60 Garden Street, Cambridge, MA 02138

<sup>3</sup> Space Research Institute, 8432 Profsojuznaya St., GSP-7, Moscow 117997, Russia

<sup>4</sup> Department of Astronomy and Astrophysics, Kavli Institute for Cosmological Physics, The Enrico Fermi Institute, 5640 South Ellis Ave., The University of Chicago, Chicago, IL 60637

the current simulations match the observed ICM profiles outside cluster cores (Nagai et al. 2006) and the global gas mass fraction (Kravtsov et al. 2006a) and are therefore sufficiently realistic for a purpose of the current study.

The mock observations of the simulated clusters are generated by exactly reproducing the response properties of the *Chandra* telescope. The analysis of the mock data is identical to that used for *real Chandra* observations by Vikhlinin et al. (2005, 2006). The comparison of the true and derived cluster properties provides an assessment of any biases introduced by the X-ray analysis. Some of these biases are potentially redshift-dependent (e.g., those related to higher merger rate or decreased ability to detect small-scale substructures in the X-ray data for high- $z$  systems). To check for any redshift dependence in such biases we use the simulation outputs at  $z = 0$  and 0.6. Our results indicate that the X-ray analysis provides accurate reconstruction of the 3D properties of the ICM. The strongest biases we find are those in the hydrostatic mass estimates. They are related to physics explicitly missing from the hydrostatic method (e.g., turbulence), and not to deficiencies of the X-ray analysis.

## 2. COSMOLOGICAL CLUSTER SIMULATIONS

In this study, we analyze high-resolution cosmological simulations of 16 cluster-sized systems in the flat  $\Lambda$ CDM model:  $\Omega_m = 1 - \Omega_\Lambda = 0.3$ ,  $\Omega_b = 0.04286$ ,  $h = 0.7$  and  $\sigma_8 = 0.9$ , where the Hubble constant is defined as  $100h \text{ km s}^{-1} \text{ Mpc}^{-1}$ , and an  $\sigma_8$  is the power spectrum normalization on an  $8h^{-1} \text{ Mpc}$  scale. The simulations were done with the Adaptive Refinement Tree (ART)  $N$ -body+gasdynamics code (Kravtsov 1999; Kravtsov et al. 2002), a Eulerian code that uses adaptive refinement in space and time, and (non-adaptive) refinement in mass (Klypin et al. 2001) to reach the high dynamic range required to resolve cores of halos formed in self-consistent cosmological simulations. The simulations presented here are discussed in detail in Kravtsov et al. (2006b) and Nagai et al. (2006) and we refer the reader to these papers for more details. Here we summarize the main parameters of the simulations.

High-resolution simulations were run using a uniform  $128^3$  grid and 8 levels of mesh refinement in the computational boxes of  $120 h^{-1} \text{ Mpc}$  for CL101–107 and  $80 h^{-1} \text{ Mpc}$  for CL3–24 (see Table 1). These simulations achieve a dynamic range of 32768 and a formal peak resolution of  $\approx 3.66 h^{-1} \text{ kpc}$  and  $2.44 h^{-1} \text{ kpc}$ , corresponding to the actual resolution of  $\approx 7 h^{-1} \text{ kpc}$  and  $5 h^{-1} \text{ kpc}$  for the  $120$  and  $80 h^{-1} \text{ Mpc}$  boxes, respectively. Only the region of  $\sim 3 - 10 h^{-1} \text{ Mpc}$  around the cluster was adaptively refined, the rest of the volume was followed on the uniform  $128^3$  grid. The mass resolution,  $m_{\text{part}}$ , corresponds to the effective  $512^3$  particles in the entire box, or the Nyquist wavelength of  $\lambda_{\text{Ny}} = 0.469 h^{-1}$  and  $0.312 h^{-1}$  comoving Mpc for CL101–107 and CL3–24, respectively, or  $0.018 h^{-1}$  and  $0.006 h^{-1} \text{ Mpc}$  in the physical units at the initial redshift of the simulations. The dark matter particle mass in the region around the cluster was  $9.1 \times 10^8 h^{-1} M_\odot$  for CL101–107 and  $2.7 \times 10^8 h^{-1} M_\odot$  for CL3–24, while other regions were simulated with lower mass resolution.

The  $N$ -body+gasdynamics cluster simulations used in this analysis include collisionless dynamics of dark matter and stars, gasdynamics and several physical processes critical to various aspects of galaxy formation: star formation, metal enrichment and thermal feedback due to supernovae Type II and Type Ia, self-consistent advection of metals, metallicity dependent radiative cooling and UV heating due to cosmo-

TABLE 1  
SIMULATED CLUSTER SAMPLE OF THE CSF RUN AT  $z=0$

Name	$r_{500c}$ ( $h^{-1} \text{ Mpc}$ )	$M_{500c}^{\text{gas}}$ ( $h^{-1} 10^{13} M_\odot$ )	$M_{500c}^{\text{tot}}$ ( $h^{-1} 10^{14} M_\odot$ )	$\langle T_{\text{spec}} \rangle^a$ (keV)
CL101 .....	1.160	8.19	9.08	8.7
CL102 .....	0.978	4.83	5.45	5.6
CL103 .....	0.993	4.93	5.71	4.7
CL104 .....	0.976	5.17	5.39	7.7
CL105 .....	0.943	4.73	4.86	6.2
CL106 .....	0.842	3.18	3.47	4.3
CL107 .....	0.762	2.17	2.57	4.0
CL3 .....	0.711	1.92	2.09	3.7
CL5 .....	0.609	1.07	1.31	1.9
CL6 .....	0.661	1.38	1.68	2.0
CL7 .....	0.624	1.22	1.41	1.9
CL9 .....	0.522	0.74	0.82	1.1
CL10 .....	0.487	0.43	0.67	2.4
CL11 .....	0.537	0.78	0.90	3.4
CL14 .....	0.509	0.62	0.77	3.0
CL24 .....	0.391	0.26	0.35	1.5

<sup>a</sup>Spectral temperature measured in the shell of  $[0.15, 1]r_{500c}$ .

logical ionizing background (Haardt & Madau 1996). The cooling and heating rates take into account Compton heating and cooling of plasma, UV heating, and atomic and molecular cooling, and are tabulated for the temperature range  $10^2 < T < 10^9 \text{ K}$  and a grid of metallicities, and UV intensities using the CLOUDY code (ver. 96b4; Ferland et al. 1998). The Cloudy cooling and heating rates take into account metallicity of the gas, which is calculated self-consistently in the simulation, so that the local cooling rates depend on the local metallicity of the gas. Star formation in these simulations was done using the observationally-motivated recipe (e.g., Kennicutt 1998):  $\dot{\rho}_* = \rho_{\text{gas}}^{1.5}/t_*$ , with  $t_* = 4 \times 10^9 \text{ yrs}$ . The code also accounts for the stellar feedback on the surrounding gas, including injection of energy and heavy elements (metals) via stellar winds, supernovae, and secular mass loss.

These simulations therefore follow the formation of galaxy clusters starting from the well-defined cosmological initial conditions and capture the dynamics and properties of the ICM in a realistic cosmological context. However, some potentially relevant physical processes, such as AGN bubbles, magnetic field, and cosmic rays, are not included. Therefore, the simulated ICM properties are probably not fully realistic in the innermost cluster regions. Moreover, the gas in the simulations is treated as an ideal inviscid fluid with a small amount of numerical viscosity, and it remains unclear to what extent the level of ICM turbulence found in the simulations and discussed below applies to real clusters. Despite these limitations, the current simulations reproduce the observed ICM profiles outside cluster cores (Nagai et al. 2006) and the global gas mass fraction (Kravtsov et al. 2006a) and are therefore sufficiently realistic for a purpose of the current study.

Our simulated sample includes 16 clusters at  $z = 0$  and their most massive progenitors at  $z = 0.6$ . The properties of simulated clusters at  $z = 0$  are given in Table 1. The masses are reported at the radius  $r_{500c}$  enclosing overdensities with respect to the critical density at the redshift of the output (below, we also use a higher overdensity level, 2500).

The mass measurement biases obviously need to be considered separately for dynamically relaxed and non-relaxed clusters. Our relaxed subsample is identified based on the overall structural morphology of their *Chandra* images, mimicking the procedure used by observers. Specifically, we visually examine mock 100 ksec images and identify “relaxed” clus-

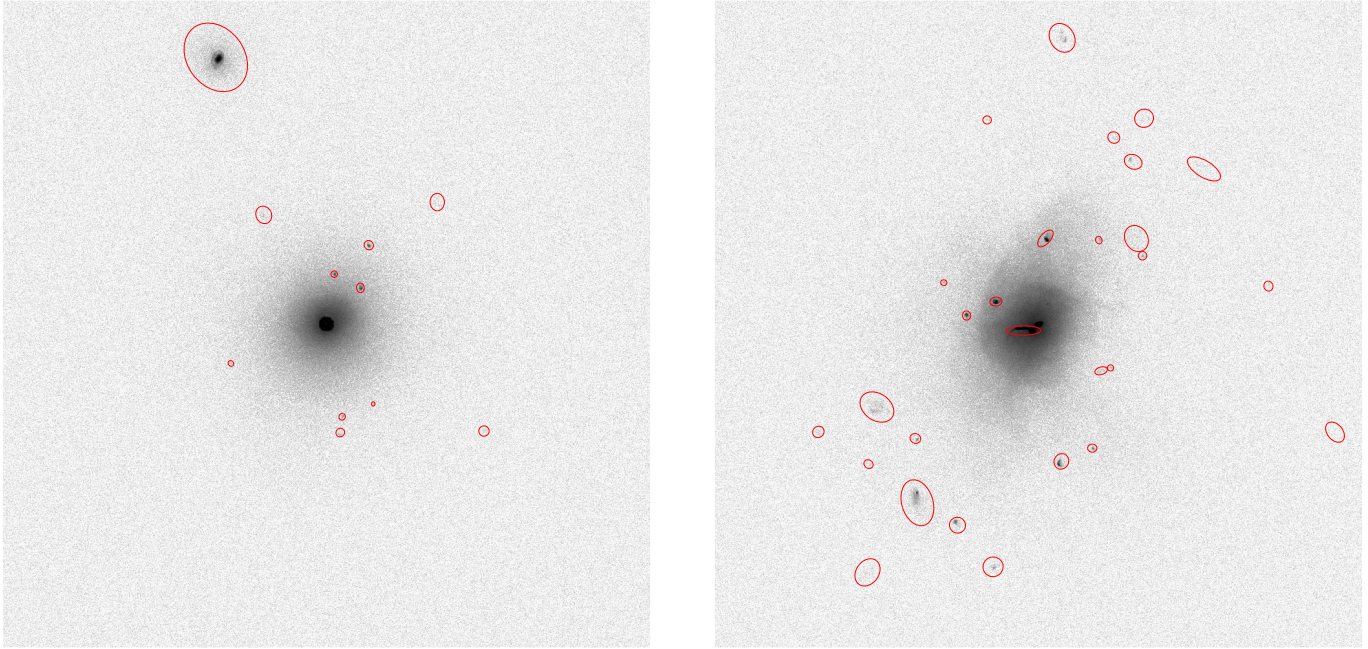


FIG. 1.— Mock *Chandra* images of the  $z = 0$  simulated clusters. The *left* and *right* panels show the images of the relaxed cluster CL104 and unrelaxed CL101, respectively. The detectable extended X-ray sources (other than the cluster itself) are detected and masked out from the analysis (red ellipses). The physical size of the images is  $5 h^{-1}$  Mpc.

ters as those with regular X-ray morphology and no secondary maxima and minimal deviations from elliptical symmetry. By contrast, “unrelaxed” clusters are those with secondary maxima, filamentary X-ray structures, or significant isophotal centroid shifts. The typical examples of systems classified as relaxed or unrelaxed are shown in Figure 1.

### 3. MOCK CHANDRA ANALYSES

#### 3.1. Simulating the Mock Chandra Data

We create X-ray flux maps of the simulated clusters viewed along three orthogonal projections. The flux map is computed by projecting X-ray emission arising from hydrodynamic cells enclosed within  $3 R_{\text{vir}}$  of a cluster along a given line-of-sight. We compute the X-ray spectrum arising from the  $i$ -th hydrodynamical cell with a cell volume  $V_i$  as

$$j_{E,i} = n_{e,i} n_{p,i} \Lambda_E(T_i, Z_i, z) V_i, \quad (1)$$

where  $n_{e,i}$ ,  $n_{p,i}$ ,  $T_i$ , and  $Z_i$  are the electron and proton densities, gas temperature, and metal abundance of the hydrodynamic cell. We compute the X-ray plasma emissivity,  $\Lambda_E(T_i, Z_i, z)$ , using the MEKAL code (Mewe et al. 1985; Kaastra & Mewe 1993; Liedahl et al. 1995) with the relative heavy element abundance from Anders & Grevesse (1989). We do not compute emission from the gas with  $T < 10^6$  K (0.086 keV) because it is below the lower limit of the *Chandra* bandpass. The plasma spectrum is multiplied by the photoelectric absorption corresponding to the hydrogen column density of  $n_H = 2 \times 10^{20} \text{ cm}^{-2}$ . The resulting map consists of  $1024 \times 1024$  2D image at 218 energy bins ranging from 0.1 to 10 keV. The pixel size is  $4.88 h^{-1}$  kpc for CL101–CL107 and  $2.44 h^{-1}$  kpc for CL3–CL24. The map size is therefore  $5 h^{-1}$  Mpc and  $2.5 h^{-1}$  Mpc, respectively. Throughout this paper, we assume the cluster redshift of  $z_{\text{obs}} = 0.06$  for the  $z = 0$  sample and  $z_{\text{obs}} = 0.6$  for the  $z = 0.6$  sample.

Next, we simulate mock *Chandra* data. We convolve the emission spectrum with the response of the *Chandra* front-illuminated CCDs and draw a number of photons at each po-

sition and spectral channel from the Poisson distribution. We simulate two sets of mock *Chandra* data. The first set has an exposure time of 100 ksec (typical for deep observations) and includes a background with the intensity corresponding to the quiescent background level in the ACIS-I observations (Markevitch et al. 2003). From these data, we generate images in the 0.7–2 keV band and use them to identify and mask out from the further analysis all detectable small-scale clumps, as routinely done by observers. Our clump detection is fully automatic and based on the wavelet decomposition algorithm described in Vikhlinin et al. (1998). Detection thresholds were chosen to allow 3–4 false detections in each image. The typical limiting flux for detection of compact extended sources is  $\sim 3 \times 10^{-15} \text{ erg s}^{-1} \text{ cm}^{-2}$  in the 0.5–2 keV band; this corresponds to a luminosity of  $\sim 1.5 \times 10^{42} \text{ erg s}^{-1}$  for clusters at  $z_{\text{obs}} = 0.06$ . Detected clumps are indicated by red ellipses in the images presented in Fig. 1. Note that the  $M_{\text{gas}}$  associated with the excluded clumps is no more than a few percent of the total enclosed  $M_{\text{gas}}$  within  $r_{500c}$  at  $z = 0.06$ . At  $z = 0.6$ , considerably smaller numbers of clumps are detected<sup>5</sup>, and the clump removal has very little effect on the analysis of high- $z$  clusters.

Once the clump detection is done on the first set, all further analysis is performed using a second set of photon maps generated for very long exposures yielding  $\approx 10^6 - 10^7$  photons outside a cluster core region in each of the simulated clusters. The exposures are artificially long by design as we are interested in exploring intrinsic limitations of the X-ray analysis, not the statistical errors due to Poisson noise in a particular choice of short exposure. Also, we ignore further complications present in reduction of real *Chandra* data, including background subtraction and spatial variations of the effective area (i.e., we assume that accurate corrections for these effects can be applied to the real data and any associated uncertainties

<sup>5</sup> Only a few clumps are detected in massive clusters with  $T_{\text{spec}} > 3 \text{ keV}$  and none in less massive systems.

are included in the reported measurement errors).

### 3.2. Analysis of Mock Chandra Data

Using the simulated mock data as an input, we repeat the analysis applied by Vikhlinin et al. (2006) and Kotov & Vikhlinin (2006) to real *Chandra* observations of relaxed clusters at  $z \approx 0$  and 0.5. The purpose of this analysis is to reconstruct spherically averaged ICM density and temperature profiles, and to estimate total cluster mass assuming hydrostatic equilibrium. The entire procedure and justification of the choices made is extensively discussed in Vikhlinin et al. (2006). Below, we briefly outline the essential steps.

The main observational input is azimuthally averaged X-ray surface brightness and projected gas temperature and metallicity profiles. The temperature and metallicity profiles are obtained from a single-temperature fit to the spectra in the 0.5–10 keV extracted in annuli with  $r_{\text{out}}/r_{\text{in}} = 1.25$  centered on a main cluster X-ray peak.

The surface brightness profiles are extracted in the 0.7–2 keV band in narrow concentric annuli ( $r_{\text{out}}/r_{\text{in}} = 1.1$ ). Using the effective area as a function of energy and observed projected temperature and metallicity at each radius, we then convert the observed *Chandra* count rate in the 0.7–2 keV band into the projected emission measure,  $EMM = \int n_e n_p dl$ .

Three-dimensional profiles of  $\rho_{\text{gas}}(r)$  and  $T_{\text{gas}}(r)$  are reconstructed by using analytic 3D models with great functional freedom, projecting them along a line of sight, and fitting the projected models to observed profiles. The gas density model we use is given by

$$n_p n_e = n_0^2 \frac{(r/r_c)^{-\alpha}}{(1 + r^2/r_c^2)^{3\beta-\alpha/2}} \frac{1}{(1 + r^\gamma/r_s^\gamma)^{\epsilon/\gamma}}. \quad (2)$$

This expression is a modification of the  $\beta$ -model (Cavaliere & Fusco-Femiano 1978) that allows independent modeling of changes in the gas density slopes in cluster cores, outskirts, and intermediate radii. Vikhlinin et al. (2006) used an additional  $\beta$ -model component with small core-radius to further increase functional freedom in a very central region. We do not use this feature and instead focus on modeling the surface brightness in a region at  $r > 0.06 \times r_{500c}$ .

The analytic expression of a 3D temperature profile was designed to model general features of observed projected temperature profiles (Vikhlinin et al. 2005). The model consists of two terms:

$$T_{3D}(r) = t(r) \times t_{\text{cool}}(r). \quad (3)$$

The first term,  $t(r)$ , describes a temperature decline at large radii by a broken power law profile with a transition region,

$$t(r) = T_0 \frac{(r/r_t)^{-a}}{(1 + (r/r_t)^b)^{c/b}}. \quad (4)$$

The second term,  $t_{\text{cool}}(r)$ , is designed to model the temperature decline in the central region affected by radiative cooling

$$t_{\text{cool}}(r) = (x + T_{\text{min}}/T_0)/(x + 1), \quad x = (r/r_{\text{cool}})^{a_{\text{cool}}}. \quad (5)$$

To fit the observed projected temperature profile, the model is projected along a line of sight. This projection requires proper weighting of multiple temperature components, and we use the algorithm that very accurately predicts a single-temperature fit to multi-component spectra in a wide range of temperatures recently proposed by Vikhlinin (2006). The observed projected temperature profiles are fit in the radial range between  $0.1r_{500c}$  and  $r_{\text{out}} = \max(1.5r_{500c}, 2/3r_{\text{max}})$ , where  $r_{\text{max}}$  is a half of the mock *Chandra* image size. The inner

radial range is set to exclude central components with unrealistic X-ray properties found in most of our simulated clusters. The exact choice of  $r_{\text{min}}$  is unimportant because we are primarily interested in the cluster properties at large radii. The choice of the outer radius is motivated by a desire to ensure accurate measurements of the temperature gradient and hence the  $M_{\text{tot}}$  at  $r_{500c}$  and that the fits in the cluster outskirts are not affected by projection effects.

Several examples of the observed surface brightness and projected temperature profiles are shown in Figures 2 and 3 along with their best fit models. We find that the models of eq.(2) and (3) usually provide an excellent description of the data, except for very irregular clusters such as that in Figure 3 (its X-ray image is shown in the right panel of Figure 1).

Given 3D models for the gas density and temperature profiles, the hydrostatic estimate of total cluster mass within a radius  $r$  is given by

$$M(r) = -\frac{T(r)r}{\mu m_p G} \left( \frac{d \log \rho_g}{d \log r} + \frac{d \log T}{d \log r} \right), \quad (6)$$

where  $\mu = 0.592$  is mean molecular weight of the fully ionized H-He plasma used in the simulations. Given  $M(r)$ , we compute the total mass at several overdensity levels,  $\Delta$ , relative to the critical density at the cluster redshift, by solving equation

$$M_\Delta(r_\Delta) = \Delta 4/3 \pi r_\Delta^3 \rho_c(z). \quad (7)$$

The ICM mass profile is obtained directly from the best-fit number density profile (eq.2),  $\rho_g = 1.236 m_p (n_p n_e)^{1/2}$ .

Finally, we compute average temperatures for each cluster using different weightings of the best-fit 3D temperature models and observed projected profiles. In this study, we consider several definitions of average temperatures. The first is a X-ray spectral temperature,  $T_{\text{spec}}$ , a value derived from a single-temperature fit to the integrated cluster spectrum excluding the core and detectable small-scale clumps. We also compute a gas-mass-weighted temperature,  $T_{\text{mg}}$ , obtained by weighting of the reconstructed temperature profile with the derived gas density profile. We also consider an emission-weighted temperature,  $T_{\text{ew}}^{\text{SIM}}$ , computed by weighting  $T(r)$  with  $n_p n_e T^{1/2}$ ; it is not directly observed but often used in the theoretical work. Similarly, we compute a true gas-mass-weighted temperature  $T_{\text{mg}}^{\text{SIM}}$  from the simulations. The superscript ‘‘SIM’’ indicates that the quantity is computed directly from the 3D gas properties in the simulations without excluding the *Chandra* detectable clumps, as opposed to from the *Chandra* analysis fits, throughout this work. All these average temperatures are computed excluding the central  $0.15 r_{500c}$  because temperatures at these radii can be strongly affected by radiative cooling and thus not directly related to the depth of the cluster potential well. Also, because of the complex physics in the innermost cluster regions the simulated ICM properties are probably not fully realistic. The outer radius of integration is set to  $r_{500c}$ , which approximately corresponds to the boundary within which the currently observed cluster temperature profiles are reliable (Vikhlinin et al. 2005). However, we also consider a spectral temperature  $T_{\text{spec}}[0.5r_{500c}]$  measured within a smaller aperture of  $0.15 < r/r_{500c} < 0.5$ ; this definition may be more practical than  $T_{\text{spec}}$  integrated out to  $r_{500c}$  for observations of limited statistical quality or spatial coverage. Note that  $T_{\text{spec}}$  is equivalent to  $T_X$  defined in Kravtsov et al. (2006b).

## 4. RESULTS



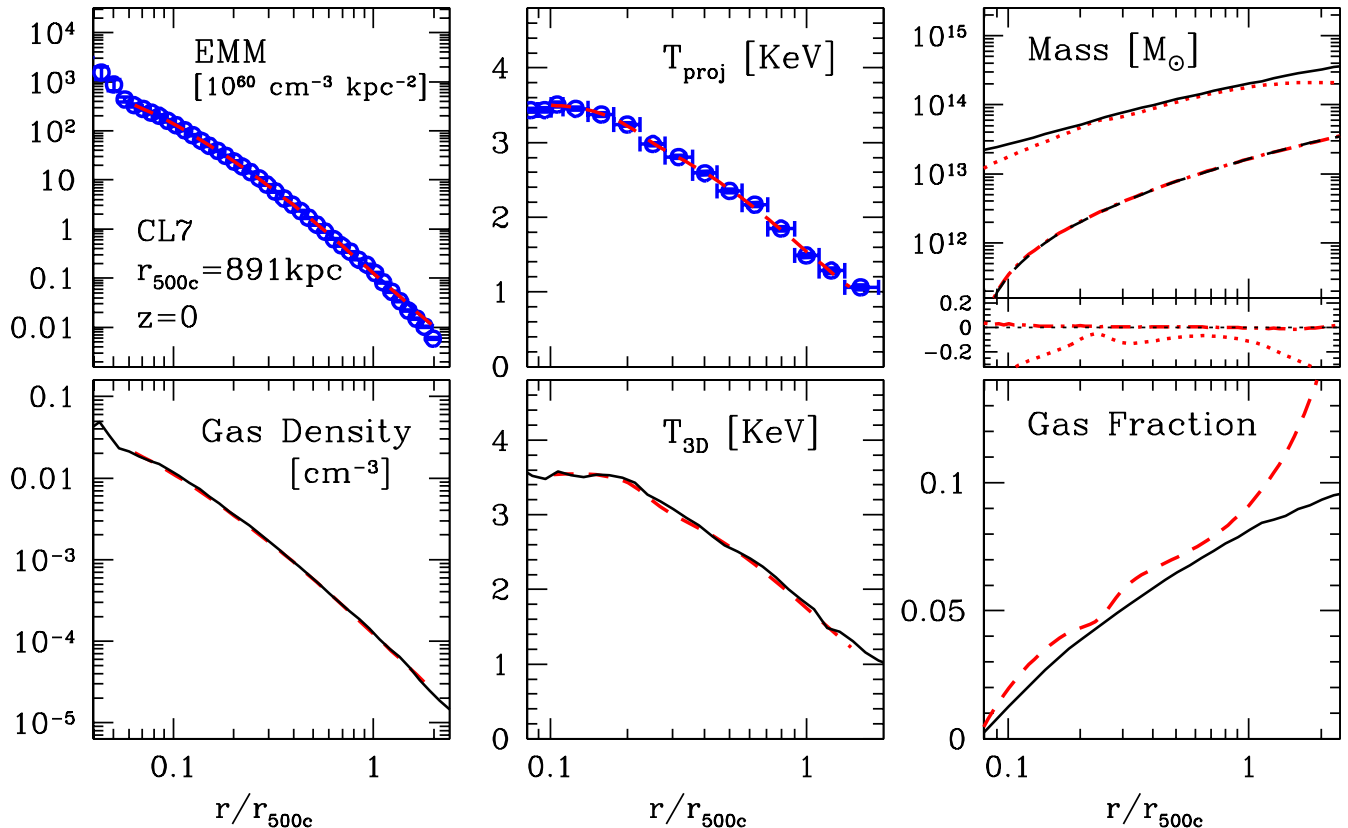


Fig. 2.— The mock *Chandra* analyses of a typical relaxed cluster, CL7, at  $z = 0$ . The cluster has  $r_{500c} = 891\text{kpc}$ ,  $M_{500c} = 1.41 \times 10^{14} h^{-1} M_{\odot}$  and  $r_{2500c} \approx 0.5r_{500c}$ . The upper-left panel shows the observed emission measure profile ( $\approx$  surface brightness). The measured projected temperature profile is shown in the upper-middle panel. In these panels, the dashed lines indicate best-fit projected profiles plotted for the radial range where the fits were made. The lower-left and -middle panels show comparisons of the best-fit 3D model profiles and true gas density and temperature profiles. Note that our model recovers well both the projected profiles and the actual 3D profiles. In the upper-right panel, we compare the derived and true  $M_{\text{tot}}$  (upper lines) and  $M_{\text{gas}}$  profiles (lower lines). The reconstructed  $M_{\text{gas}}$  profile (dot-dashed line) is accurate to a few percent in the entire radial range shown. The hydrostatic  $M_{\text{tot}}$  estimate (dotted line), on the other hand, is biased low by about 5%–10% in the radial range,  $[0.2, 1.0]r_{500c}$ . The lower-right shows that measured cumulative  $f_{\text{gas}}$  is biased high by  $\approx 10\%$  in the radial range of  $[0.2, 1.0]r_{500c}$  for this cluster, and it is primarily due to the bias in the hydrostatic mass estimate.

#### 4.1. Profiles of Relaxed clusters

Figure 2 shows the profile analysis of one of the relaxed clusters, CL7, at  $z = 0$ . The upper-left panel shows the emission measure (EMM) profile constructed from the mock *Chandra* photon map. The dashed line is a best-fit model in the radial range between  $0.06r_{500c}$  and  $2r_{500c}$ . In this radial range, the EMM profile is very smooth and the model provides an excellent fit. We do not model an additional component associated with dense and cool gas in the inner  $\approx 50$  kpc. Note, however, that the  $M_{\text{gas}}(<50 \text{ kpc})$  is only a small fraction ( $\approx 2\%$ ) of the  $M_{\text{gas}}(<r_{500c})$ .

The upper-middle panel shows the projected temperature profile obtained from the X-ray spectral fitting at each projected annulus. Data points are plotted as a function of X-ray counts weighted radius, and the error bars in the horizontal axis indicate a radial bin size within which the X-ray spectrum was extracted. The best-fit profile, indicated by the dashed line, is a very good description of the data in  $0.1 < r/r_{500c} < 1.5$ , the radial range where the fit was done.

In the lower-left and lower-middle panels, we compare the best-fit model profiles from the mock *Chandra* analysis to the true 3D gas density and temperature profiles measured in the simulation. For the true profiles, we compute a density profile of hot, X-ray emitting gas with  $T > 10^6$  K and a gas-mass-weighted temperature. Note that a volume-averaged tempera-

ture is quite similar to the gas-mass-weighted average shown here. For this cluster, both 3D gas density and temperature profiles are recovered very accurately.

The upper-right panel shows the comparisons of the  $M_{\text{tot}}$  and  $M_{\text{gas}}$  profiles derived from the mock *Chandra* analysis and their respective true profiles. The comparisons show that the  $M_{\text{gas}}$  profile is unbiased, and it is recovered to better than 2% in  $0.1 < r/r_{500c} < 2$ , nearly the entire radial range where the EMM profile was modeled. The  $M_{\text{tot}}$  derived from hydrostatic mass modeling, on the other hand, is biased low by about 5%–10% in the radial range of  $0.2 < r/r_{500c} < 1$ . The figure also shows that the measured  $f_{\text{gas}}$  is biased high, on average, by about 10% at all radii, mainly due to the bias in the hydrostatic estimate of  $M_{\text{tot}}$ .

These results are representative of those for other clusters in the relaxed cluster samples at both  $z = 0$  and 0.6. The 3D gas density and temperature profiles are recovered remarkably well, and the  $M_{\text{gas}}$  profiles are accurate to a few per cent at all radii. The  $M_{\text{tot}}$ , on the other hand, is typically biased low by about 5%–20% throughout the clusters. One exception is the  $M_{\text{tot}}$  measurement for one of the most relaxed clusters, CL104, at  $z = 0$ , which is nearly unbiased. This system has not experienced a major merger for several dynamical time ( $\approx 6$  Gyr).

#### 4.2. Profiles of Unrelaxed Clusters

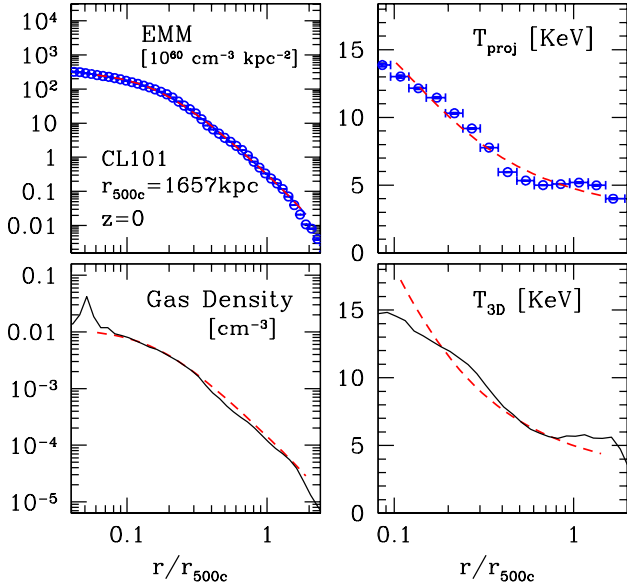


FIG. 3.— Same as Fig. 2, but for one of the unrelaxed clusters, CL101 at  $z = 0$ . The emission measure and projected temperature profiles exhibit bumps and wiggles. The derived  $M_{\text{gas}}$  and  $M_{\text{tot}}$  profiles are thus less accurate than those in relaxed systems. However, the fits to the projected data are still good, highlighting the flexibility of our gas density and temperature models.

Accurate  $M_{\text{tot}}$  estimates in unrelaxed clusters cannot be obtained from the hydrostatic equilibrium assumption. Reconstruction of 3D gas mass and temperature profiles from projected X-ray data can be done only approximately in such systems because of deviations from spherical symmetry. However, many applications (e.g., cluster mass function estimates) require analyses of full statistical samples that include both relaxed and unrelaxed systems. It is therefore important to ask how well the observational analysis procedures can recover properties of the ICM for unrelaxed systems.

Unrelaxed clusters are a diverse population with a wide range of dynamical states. For the purpose of illustration, we show the profile analysis for a cluster undergoing a major merger, CL101 at  $z = 0$  (Fig.3). This example highlights salient features of unrelaxed systems. Compared to relaxed clusters, their EMM and projected temperature profiles are less smooth and exhibit more pronounced bumps and wiggles. These features are not recovered by our smooth 3D model, even though the overall trends in the projected temperature and especially in the EMM are reproduced reasonably well. Recovery of the 3D gas density and temperature profiles is much less accurate than for relaxed systems. In the case of CL101, for example, the derived  $M_{\text{gas}}$  profile is biased high by about 5%–10% at all radii, and the 3D temperature profile is biased low at  $r > 0.1r_{500c}$ . If the hydrostatic equation is blindly applied to the best-fit models, the derived  $M_{\text{tot}}$  is biased low by 25% at  $r_{500c}$ .

#### 4.3. Gas Mass, Total Mass and Gas Mass Fractions

In this section, we assess biases in the X-ray estimates of the enclosed  $M_{\text{tot}}$ ,  $M_{\text{gas}}$ , and  $f_{\text{gas}}$ . The bias is defined as a fractional difference between estimated mass,  $M_{\text{est}}$ , derived from the mock *Chandra* analysis and true 3D mass,  $M_{\text{true}}$ , measured directly in simulations,  $\text{bias} = (M_{\text{est}} - M_{\text{true}})/M_{\text{true}}$ . Figure 4 shows the results for all simulated clusters at  $z = 0$  and at radii enclosing two different overdensities:  $r_{2500c}^{\text{true}}$  and

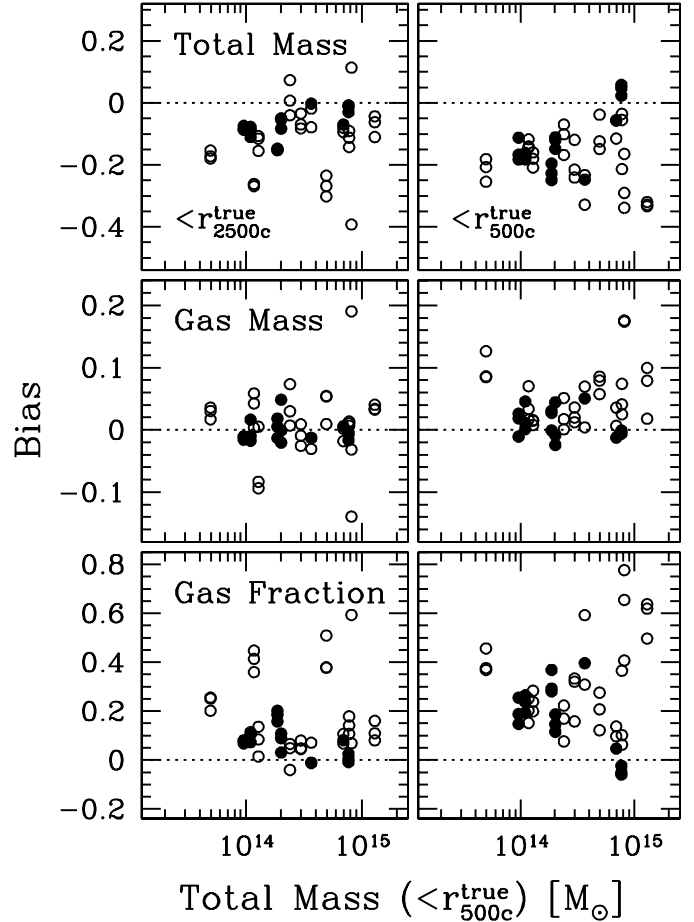


FIG. 4.— Bias in the  $M_{\text{tot}}$ ,  $M_{\text{gas}}$ , and  $f_{\text{gas}}$  measured within  $r_{500c}^{\text{true}}$  (left) and  $r_{2500c}^{\text{true}}$  (right) for simulated clusters at  $z = 0$ . The bias is defined as, e.g.,  $(M_{\text{est}} - M_{\text{true}})/M_{\text{true}}$ , where both  $M_{\text{est}}$  and  $M_{\text{true}}$  are at the same radius. Each cluster is viewed along three orthogonal projections, and clusters with relaxed and unrelaxed morphologies are indicated with *filled* and *open* symbols, respectively.

$r_{500c}^{\text{true}}$ . Both estimated ( $M_{\text{est}}$ ) and true masses ( $M_{\text{true}}$ ) are measured in the same physical region enclosed within “true” radii ( $r_{\text{true}}$ ) measured directly from simulations. Note also that the  $M_{\text{gas}}$  is computed by excluding the mass enclosed within  $0.075r_{500c}^{\text{true}6}$  (from both true and estimated masses), while the  $M_{\text{tot}}$  is obtained without excluding the central region. The  $f_{\text{gas}} \equiv M_{\text{gas}}/M_{\text{tot}}$  is therefore a fraction computed using these two quantities measured in a slightly different radial range. Table 2 also summarizes average biases and scatter in the mass estimates at both  $z = 0$  and 0.6.

The upper panels in Figure 4 show that the hydrostatic mass estimate is typically biased low. It is underestimated on average by 12% at  $r_{2500c}^{\text{true}}$  and 16% at  $r_{500c}^{\text{true}}$  for all clusters at  $z = 0$ . The bias in the hydrostatic mass is smaller in the inner region and it increases toward cluster outskirts. The bias is also smaller in relaxed systems than in unrelaxed systems; for example, biases are 8% and 15% at  $r_{2500c}^{\text{true}}$  for the relaxed and unrelaxed samples, respectively. Note also that the scatter is very small inside  $r_{2500c}^{\text{true}}$  of the relaxed clusters. These results indicate that the hydrostatic condition is best realized in

<sup>6</sup> The choice is made to ensure that the central, dense and cool gas component, associated with the ISM of the central cluster galaxy, is excluded from the  $M_{\text{gas}}$  estimates of all clusters. This gas contributes  $\lesssim 2\%$  of the total  $M_{\text{gas}}$ .

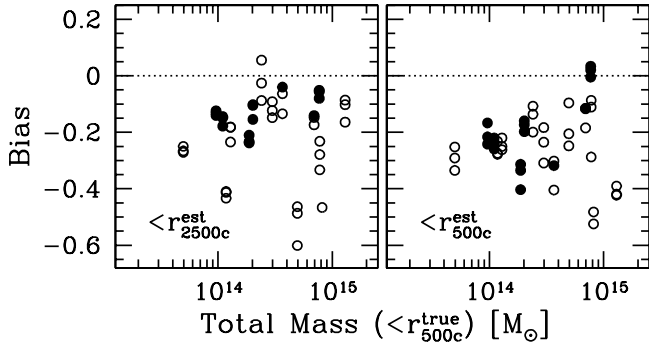


FIG. 5.— Same as the upper-panels in Fig. 4, except that the estimated mass ( $M_{\text{est}}$ ) is evaluated within the estimated virial radii ( $r_{\text{est}}$ ); hence,  $M_{\text{est}}$  and  $M_{\text{true}}$  are measured in different physical regions.

the inner region of relaxed clusters, while the deviation from the hydrostatic equilibrium become more prominent in cluster outskirts and/or unrelaxed systems, as expected. Similar results are obtained for clusters at high redshift.

The middle panels in Figure 4 illustrate that the X-ray gas mass determinations are remarkably accurate and robust. The  $M_{\text{gas}}$  measurements are accurate to better than a few percent for both relaxed and unrelaxed clusters and independent of redshift. For the relaxed cluster samples, the accuracy of the  $M_{\text{gas}}$  measurements is as good as 1% at  $r_{500c}^{\text{true}}$  with 3%  $1\sigma$  scatter. Although the effect is small ( $\lesssim 6\%$ ), the  $M_{\text{gas}}$  is biased high in the outskirts of the unrelaxed systems.

The lower panels of Figure 4 show the biases in measurements of the gas mass fractions. Since the hydrostatic mass is biased low, the derived  $f_{\text{gas}}$  are typically biased high. The bias and scatter in  $f_{\text{gas}}$  are especially large for the unrelaxed clusters, since the biases in  $M_{\text{gas}}$  and  $M_{\text{tot}}$  are added constructively. Both bias and scatter are significantly reduced for relaxed clusters; for example,  $f_{\text{gas}}(\langle r_{2500c}^{\text{true}} \rangle)$  are accurate to about 10% at  $z = 0$  and 0.6. The biases become larger in cluster outskirts, and the biases in  $f_{\text{gas}}(\langle r_{500c}^{\text{true}} \rangle)$  are about 18% at both low and high redshifts.

In practice, additional biases in the estimated cluster masses ( $M_{\text{est}}$ ) could arise from a bias in the estimation of a cluster virial radius. Figure 5 shows the biases in the estimated hydrostatic mass within the estimated virial radius,  $M_{\text{est}}(\langle r_{\text{est}} \rangle)$ , relative to the true cluster mass,  $M_{\text{true}}(\langle r_{\text{true}} \rangle)$ , measured in simulations. The column indicated as  $M_{\text{tot}}(\langle r_{\text{est}} \rangle)$  in Table 2 summarizes average biases and scatter in the estimates of total cluster masses computed this way. An underestimate of a cluster virial radius results in the increased bias in the  $M_{\text{tot}}$  estimate and an underestimate of the derived  $M_{\text{gas}}$  by a similar amount, while leaving  $f_{\text{gas}}$  relatively unchanged. It is these errors that contribute to the differences in the mass-temperature relations discussed in § 4.5.

A similar study of biases in the hydrostatic  $M_{\text{tot}}$  estimates has been done recently by Rasia et al. (2006). The cosmological simulations were performed using the Gadget-2 SPH code (Springel 2005) and the mock X-ray data were reduced closely following the procedure of Ettori et al. (2002). Their sample included 5 clusters, including two with relaxed morphology, for which the comparison with our results is most relevant. The mass biases in the most comparable case (direct hydrostatic estimates and reduced *Chandra* background level) are  $-30\%$  and  $-28\%$  at  $r_{2500c}$ , and  $-15\%$  and  $-32\%$  at  $r_{500c}$ . These values are on the lower side of our distribution for relaxed clusters (Fig.4). In particular, none of

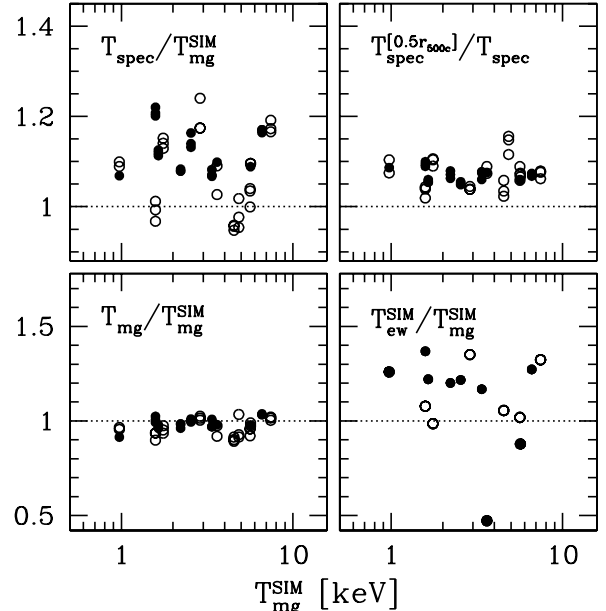


FIG. 6.— Comparisons of various average ICM temperatures for the  $z = 0$  sample. The temperature averages are defined in the text. The filled and open symbols indicate clusters with relaxed and unrelaxed morphology, respectively. For each cluster results for the three projections are shown.

our relaxed clusters shows such strong biases at  $r = r_{2500c}$ . However, it is difficult to compare our results directly. Not only the cosmological simulation codes are quite different, but also the data analysis algorithms are completely independent and significantly different. Investigations of the sources of discrepancy will require cross-checks (e.g., reduction of our mock data with the Rasia et al. pipeline) and/or using a larger sample of Gadget-2 clusters.

#### 4.4. Average Temperatures

Average cluster temperature,  $\langle T \rangle$ , is another important ICM diagnostic and a key observable for cosmological application. Since the ICM is not isothermal within a cluster, the definition of  $\langle T \rangle$  is not unique. The differences among various definitions should be calibrated and taken into account. Figure 6 compares different  $\langle T \rangle$  obtained from the mock *Chandra* analysis,  $T_{\text{spec}}$ ,  $T_{\text{spec}}^{[0.5r_{500c}]}$ , and  $T_{\text{mg}}$ , as well as those measured directly from the 3D properties of gas in simulations,  $T_{\text{ew}}^{\text{SIM}}$  and  $T_{\text{mg}}^{\text{SIM}}$ , for all clusters at  $z = 0$  and 0.6 (see § 3.2). The gas with  $T < 0.086$  keV ( $10^6$  K) is excluded from all calculations of average temperatures, since it does not contribute to the X-ray flux. Note also that detectable small clumps are excluded from the mock *Chandra* analysis and hence do not affect the determination of  $\langle T \rangle$ . Average ratios of different temperature definitions are summarized in Table 3.

The best agreement is between the true and X-ray derived gas mass-weighted temperatures. Other definitions show a constant offset relative to  $T_{\text{mg}}^{\text{SIM}}$  with some scatter around the mean. For the relaxed clusters at  $z = 0$ , we find  $T_{\text{ew}}^{\text{SIM}} : T_{\text{spec}} : T_{\text{mg}} : T_{\text{mg}}^{\text{SIM}} = 1.19 : 1.13 : 0.99 : 1$ . The ratios are slightly different for the non-relaxed clusters,  $T_{\text{ew}}^{\text{SIM}} : T_{\text{spec}} : T_{\text{mg}} : T_{\text{mg}}^{\text{SIM}} = 0.99 : 1.07 : 0.96 : 1$ . The  $T_{\text{spec}}$  is higher than  $T_{\text{mg}}$  because the former is dominated by the inner, hotter region

TABLE 2  
BIAS IN  $M_{\text{tot}}$ ,  $M_{\text{gas}}$  AND  $f_{\text{gas}}$  MEASUREMENTS.

Redshift	Radial range	Sample	Bias $\pm$ Scatter			
			$M_{\text{tot}}(< r_{\text{true}})^{\text{a}}$	$M_{\text{tot}}(< r_{\text{est}})^{\text{a}}$	$M_{\text{gas}}^{\text{b}}$	$f_{\text{gas}}^{\text{c}}$
$z = 0$	$< r_{2500c}$	all	$-0.121 \pm 0.136$	$-0.222 \pm 0.181$	$0.006 \pm 0.047$	$0.202 \pm 0.431$
		relaxed	$-0.075 \pm 0.047$	$-0.134 \pm 0.059$	$-0.003 \pm 0.017$	$0.091 \pm 0.062$
		unrelaxed	$-0.146 \pm 0.163$	$-0.270 \pm 0.207$	$0.010 \pm 0.056$	$0.268 \pm 0.525$
$z = 0$	$< r_{500c}$	all	$-0.163 \pm 0.095$	$-0.253 \pm 0.162$	$0.041 \pm 0.048$	$0.264 \pm 0.184$
		relaxed	$-0.130 \pm 0.096$	$-0.195 \pm 0.124$	$0.011 \pm 0.023$	$0.176 \pm 0.136$
		unrelaxed	$-0.182 \pm 0.091$	$-0.285 \pm 0.173$	$0.058 \pm 0.051$	$0.312 \pm 0.190$
$z = 0.6$	$< r_{2500c}$	all	$-0.122 \pm 0.116$	$-0.245 \pm 0.151$	$0.010 \pm 0.045$	$0.175 \pm 0.216$
		relaxed	$-0.100 \pm 0.024$	$-0.178 \pm 0.038$	$0.000 \pm 0.022$	$0.112 \pm 0.038$
		unrelaxed	$-0.135 \pm 0.145$	$-0.286 \pm 0.178$	$0.016 \pm 0.054$	$0.213 \pm 0.266$
$z = 0.6$	$< r_{500c}$	all	$-0.089 \pm 0.206$	$-0.144 \pm 0.306$	$0.024 \pm 0.072$	$0.180 \pm 0.272$
		relaxed	$-0.152 \pm 0.069$	$-0.214 \pm 0.079$	$0.007 \pm 0.029$	$0.196 \pm 0.111$
		unrelaxed	$-0.052 \pm 0.250$	$-0.102 \pm 0.379$	$0.034 \pm 0.087$	$0.171 \pm 0.335$

<sup>a</sup>Estimated masses,  $M_{\text{est}}$ , enclosed within  $r_{\text{true}}$  and  $r_{\text{est}}$  are compared with true cluster masses,  $M_{\text{true}}(< r_{\text{true}})$ , measured in simulations.

<sup>b</sup>Enclosed  $M_{\text{gas}}$  within  $r_{500c}$  and  $r_{2500c}$  excluding the mass enclosed within  $0.075r_{500c}$ .

<sup>c</sup>A fraction computed using above two quantities.

TABLE 3  
RATIO OF AVERAGE CLUSTER GAS TEMPERATURES

Redshift	Sample	Average $\pm$ Scatter			
		$T_{\text{mg}}/T_{\text{mg}}^{\text{SIM}}$	$T_{\text{spec}}/T_{\text{mg}}^{\text{SIM}}$	$T_{\text{ew}}^{\text{SIM}}/T_{\text{mg}}^{\text{SIM}}$	$T_{\text{spec}}^{[0.5r_{500c}]} / T_{\text{spec}}$
$z = 0$	all	$0.973 \pm 0.040$	$1.095 \pm 0.078$	$1.078 \pm 0.283$	$1.072 \pm 0.027$
	relaxed	$0.990 \pm 0.029$	$1.126 \pm 0.049$	$1.188 \pm 0.192$	$1.070 \pm 0.015$
	unrelaxed	$0.960 \pm 0.042$	$1.070 \pm 0.087$	$0.992 \pm 0.315$	$1.073 \pm 0.034$
$z = 0.6$	all	$0.985 \pm 0.047$	$1.080 \pm 0.075$	$1.511 \pm 0.619$	$1.044 \pm 0.019$
	relaxed	$0.985 \pm 0.029$	$1.110 \pm 0.056$	$1.725 \pm 0.789$	$1.048 \pm 0.007$
	unrelaxed	$0.985 \pm 0.054$	$1.066 \pm 0.079$	$1.404 \pm 0.459$	$1.042 \pm 0.022$

(see examples of the temperature profiles in Fig. 2 and 3). A tight correlation exists between  $T_{\text{spec}}$  and  $T_{\text{mg}}^{\text{SIM}}$  with the object-to-object scatter as small as 5% for the relaxed clusters and 9% even for the unrelaxed systems. Although computed directly from the simulation outputs,  $T_{\text{ew}}^{\text{SIM}}$  shows a much poorer correlation with  $T_{\text{mg}}^{\text{SIM}}$  than any of the observationally derived average temperatures. The scatter in the temperature ratios is generally higher for non-relaxed systems.

The X-ray spectral temperature,  $T_{\text{spec}}$ , is of particular interest to X-ray observers, because it is the most easily measured spectral characteristic. Our study shows that  $T_{\text{spec}}$  is related to  $T_{\text{mg}}$  by a constant factor,  $T_{\text{spec}}/T_{\text{mg}} \approx 1.14$ , for the relaxed clusters and a slightly smaller factor,  $T_{\text{spec}}/T_{\text{mg}} = 1.12$ , in the unrelaxed systems. For each sub-sample, the ratio  $T_{\text{spec}}/T_{\text{mg}}$  and its scatter are nearly identical at  $z = 0$  and 0.6 and do not show any sign of evolution with redshift. Similar results are obtained for  $T_{\text{spec}}^{[0.5r_{500c}]}$ , which is related to  $T_{\text{spec}}$  by a constant factor,  $T_{\text{spec}}^{[0.5r_{500c}]} / T_{\text{spec}} \approx 1.04 - 1.07$  with little redshift trend and scatter, indicating that  $T_{\text{spec}}^{[0.5r_{500c}]}$  can be used as a reliable substitute for  $T_{\text{spec}}$ . Finally, the ratio of  $T_{\text{spec}}/T_{\text{mg}}$  and its scatter from cosmological simulations is in good agreement with the *Chandra* results for low-redshift relaxed clusters (Vikhlinin et al. 2006), where the average ratio in  $[0.15, 1]r_{500c}$  is 1.15 and scatter is about 0.08.

#### 4.5. Implications for the Mass-Temperature relation

The results in § 4.3–4.4 have direct implications for the mass-temperature ( $M - T$ ) relation. The normalization of the

$M - T$  relation,  $M_5$ , can be defined as

$$E(z) M_{500c} = M_5 \left( \frac{\langle T \rangle}{5 \text{ keV}} \right)^{3/2} \quad (8)$$

where  $E(z) = (\Omega_M(1+z)^3 + \Omega_\Lambda)^{1/2}$  for a flat universe with a cosmological constant. Table 4 lists the best-fit values of  $M_5$  and its uncertainties (arising because of the finite sample size) for different temperature averages (see also Table 2 and Fig. 6 in Kravtsov et al. 2006b). The values of  $M_5$  are computed using both the true mass,  $M_{500c}^{\text{true}}(< r_{500c}^{\text{true}})$ , measured in simulations and the estimated mass,  $M_{500c}^{\text{est}}(< r_{500c}^{\text{est}})$ , derived from the mock analysis. For  $M_{500c}^{\text{true}}$ , the  $M_5$  is higher by about 10% than their observed counterparts at both low and high-redshifts:  $M_5 = 3.06 \pm 0.16$  ( $T_{\text{spec}}$ ) and  $3.64 \pm 0.18$  ( $T_{\text{mg}}$ ) at  $z \sim 0$  (Vikhlinin et al. 2006) and  $M_5 = 3.36 \pm 0.32$  ( $T_{\text{spec}}$ ) at  $z \sim 0.5$  (Kotov & Vikhlinin 2006).<sup>7</sup> The  $M_5$  based on  $M_{500c}^{\text{est}}$ , on the other hand, is lower by about 10%–15%. In other words, the observed relations lie between the simulations derived relations based on the true and estimated masses.

## 5. DISCUSSION AND CONCLUSIONS

We present mock *Chandra* analyses of cosmological cluster simulations and assess X-ray measurements of galaxy cluster properties. To test observational X-ray procedures, we construct mock *Chandra* images of the simulated clusters and

<sup>7</sup> To compare the M-T relations from simulations and observations in the same radial range ( $0.15r_{500c} - r_{500c}$ ), we applied the correction factors of  $\langle T(0.15r_{500c} - r_{500c}) \rangle / \langle T(70 \text{ kpc} - r_{500c}) \rangle = 0.97$  (for  $T_{\text{spec}}$ ) and 0.94 (for  $T_{\text{mg}}$ ) to the observed relations.



TABLE 4  
NORMALIZATIONS OF THE  $M_{500c} - T$  RELATION

Mass <sup>a</sup>	Redshift	Sample	$M_5, 10^{14} h^{-1} M_\odot$		
			$T_{\text{mg}}$	$T_{\text{spec}}$	$T_{\text{spec}}^{[0.5r_{500c}]}$
$M_{500c}^{\text{true}}$	$z = 0$	all	$4.46 \pm 0.18$	$3.78 \pm 0.21$	$3.40 \pm 0.17$
		relaxed	$4.02 \pm 0.10$	$3.32 \pm 0.10$	$3.00 \pm 0.09$
		unrelaxed	$4.80 \pm 0.19$	$4.14 \pm 0.22$	$3.71 \pm 0.18$
$M_{500c}^{\text{true}}$	$z = 0.6$	all	$4.65 \pm 0.17$	$4.07 \pm 0.17$	$3.81 \pm 0.16$
		relaxed	$4.50 \pm 0.12$	$3.77 \pm 0.12$	$3.51 \pm 0.12$
		unrelaxed	$4.73 \pm 0.18$	$4.22 \pm 0.17$	$3.96 \pm 0.16$
$M_{500c}^{\text{est}}$	$z = 0$	relaxed	$3.14 \pm 0.03$	$2.59 \pm 0.03$	$2.35 \pm 0.04$
$M_{500c}^{\text{est}}$	$z = 0.6$	relaxed	$3.55 \pm 0.07$	$2.97 \pm 0.06$	$2.77 \pm 0.06$

<sup>a</sup> $M_{500c}^{\text{true}}$  is the true  $M_{\text{tot}}$  of a cluster enclosed within the true  $r_{500c}^{\text{true}}$  measured directly in simulations;  $M_{500c}^{\text{est}}$  is the estimated hydrostatic mass enclosed within the estimated  $r_{500c}^{\text{est}}$  from the mock data analysis.

derive properties of X-ray clusters using a model and procedure essentially identical to those used in real data analysis. The sample includes 16 clusters spanning a broad mass range ( $5 \times 10^{13} - 2 \times 10^{15} h^{-1} M_\odot$ ) simulated in the  $\Lambda$ CDM cosmology with high spatial resolution and including various physical processes of galaxy formation, such as radiative cooling, star formation and other processes accompanying galaxy formation. We analyze the simulated clusters at  $z = 0$  and their most massive progenitors at  $z = 0.6$ . To test the sensitivity of the X-ray analysis to the cluster dynamical state and substructure, we also distinguish unrelaxed clusters from relaxed systems based on the overall structural morphology of the *Chandra* images, as usually done to classify observed clusters. Below we discuss and summarize our main findings and conclusions.

### 5.1. Reconstruction of 3D ICM Properties

Derivation of the cluster 3D properties from projected X-ray data usually relies on simplifying assumptions such as spherical symmetry of a cluster or small-scale uniformity of the ICM. Additional complications arise from a non-ideal response of X-ray telescopes and limited statistical quality of data. This leads to several effects which are hard to reproduce analytically without creating mock X-ray data from realistic cluster simulations. For example, clumps of colder gas associated with massive subhalos can be detected and masked out from a further analysis while smaller subhalos remain undetected and bias projected temperature and X-ray brightness measurements (Mazzotta et al. 2004; Vikhlinin 2006). One of the goals of our work is to include all such effects as completely as possible in generation of the mock X-ray data and thus to test how they bias X-ray measurements and recovery of 3D ICM profiles.

Reassuringly, we find that the ICM models and analysis method presented in Vikhlinin et al. (2006) provide a good description of emission measure and projected temperature profiles of the ICM. For relaxed clusters, these models recover the 3D gas density, temperature, and gas mass profiles with the accuracy of a few percent at  $0.1 < r/r_{500c} < 2.0$ . The models are flexible enough to describe also non-relaxed systems and provide reasonably accurate gas mass and temperature measurements. A practical implication of these results is that projection effects, cluster substructure, and deviations from spherical symmetry do not strongly affect reconstruction of 3D ICM density, temperature, pressure, and entropy profiles from X-ray data. Therefore, observational results on

ICM profiles can be directly compared to the properties of simulated clusters without a need for detailed mock X-ray analyses. Such a comparison for our sample will be presented in the future paper (Nagai et al. 2006).

The total ICM mass is measured quite accurately in all our simulated clusters. Results are most accurate for relaxed systems: biases and scatter in  $M_{\text{gas}}$  measurements are accurate to better than  $\sim 3\%$  percent, independent of a cluster redshift or a radial range within in which the  $M_{\text{gas}}$  is measured. For unrelaxed systems, the scatter is larger, as expected (Mathiesen et al. 1999), but the bias is still small ( $\lesssim 10\%$ ).

Average temperature is an important diagnostic of properties and physical processes of the ICM and a key observable for cosmological applications. Since clusters are not isothermal, the definition of the  $\langle T \rangle$  is not unique nor can  $\langle T \rangle$  be completely accurately derived from data. Mock X-ray analysis is therefore required to study the relation among different  $\langle T \rangle$  definitions used in observational and theoretical studies. Our analysis is focused on the comparisons of the true gas-mass-weighted average temperature,  $T_{\text{mg}}^{\text{SIM}}$ , and the X-ray spectroscopic  $T_{\text{spec}}$  or gas-mass-weighted  $T_{\text{mg}}$  temperatures derived from the mock data. We find that these temperatures are not identical, but the difference is mostly a constant factor with a relatively small object-to-object scatter. For example,  $T_{\text{spec}}/T_{\text{mg}} \approx 1.14 \pm 0.05$  for relaxed clusters, while for unrelaxed objects this ratio is  $T_{\text{spec}}/T_{\text{mg}} \approx 1.12 \pm 0.09$ . All the  $\langle T \rangle$  definitions we tested are therefore equivalent, but the difference should be kept in mind when, e.g., observed  $M - T$  relations are compared with results of simulations. A notable exception is the ‘‘emission-weighted’’ temperature defined as  $T_{\text{ew}} = \int T \rho^2 T^{1/2} dV / \int \rho^2 T^{1/2} dV$  (Bryan & Norman 1998; Frenk et al. 1999; Muanwong et al. 2001). Even computed directly from the simulation outputs, this quantity shows a much poorer correlation with  $T_{\text{mg}}^{\text{SIM}}$  than any of the observationally derived average temperatures (Fig.6). Our results thus support the suggestion of Mazzotta et al. (2004) that  $T_{\text{ew}}$  should not be used as a measure of the average cluster temperature.

### 5.2. Accuracy of Hydrostatic Mass Estimates

One of the major applications of the gas density and temperature profile measurements from the X-ray data is the estimate of a gravitationally bound mass of a cluster assuming that the ICM is in hydrostatic equilibrium in the cluster potential. The X-ray method is by far the most precise way to estimate  $M_{\text{tot}}$  in individual objects at large radii. This limits our ability to test biases in the X-ray derived  $M_{\text{tot}}$  estimates through comparisons with independent observational techniques such as weak lensing. The analysis of our mock X-ray data, however, provides important clues.

We find that the hydrostatic mass estimates from our mock data are biased low by about 5%–20% throughout the virial region (Fig.4), even in clusters that are identified as relaxed by their X-ray morphology. Such biases seem to be too high to be attributed to inaccuracies in 3D gas density and temperature profile reconstruction. A more plausible explanation is a departure of the ICM from a hydrostatic state. Indeed, an additional pressure component due to residual random bulk motions of the ICM in our simulated clusters completely explains the bias in the hydrostatic mass estimates (this topic will be discussed in greater detail in Lau et al. 2006). Similar results have been also obtained by independent simulations performed with different codes and implementation of physical processes (Rasia et al. 2006; Dolag et al. 2005). The

$M_{\text{tot}}$  bias derived in the mock X-ray analysis of our relaxed clusters increases towards their outskirts. The average levels are  $-8\%$  at  $r = r_{2500c}$  and  $-13\%$  at  $r = r_{500c}$ , and quickly become very large beyond  $r_{500c}$  (Fig.2), which qualitatively mimic the radial dependence of turbulent pressure observed in previous simulations (e.g., Evrard et al. 1996). In unrelaxed clusters, not only the departures from hydrostatic equilibrium are strong but also the density and temperature gradients are not measured accurately (Fig.3) resulting in  $M_{\text{tot}}$  biases of 20% or more at all radii.

It is unclear to what degree the level of ICM turbulence found in these simulations applies to real clusters because most of the codes model ICM as an ideal inviscid fluid with some amount of numerical viscosity. Further progress in this area using cosmological simulations will have to rely on better understanding and modeling of viscosity of the weakly magnetized plasma (Ruszkowski et al. 2004a,b; Dolag et al. 2005; Sijacki & Springel 2006). Direct measurements of the ICM turbulence through Doppler broadening of emission lines (Inogamov & Sunyaev 2003) must await a launch of X-ray calorimeters, although some clues could be provided also by observations of X-ray brightness fluctuations (Schuecker et al. 2004). Keeping these uncertainties in mind, we can treat the  $M_{\text{tot}}$  biases quoted above as upper limits.

Cosmic rays and magnetic fields may also provide non-thermal pressure support which is not accounted for in the hydrostatic estimates nor included in our simulations. In addition, temperatures of electron and ion components of the ICM are not necessarily the same, because strong shocks heat primarily ions and the collisional electron-ion equilibration time is long in the cluster outskirts (Markevitch et al. 1996; Fox & Loeb 1997). If  $T_e$  (derived from X-ray spectra) is indeed lower than  $T_i$  (unobserved), the hydrostatic mass estimates are biased low. We note, however, that at least in one case there is evidence for fast equilibration of the electron and ion temperatures in a post-shock region of the ICM (Markevitch 2005).

While direct measurements or theoretical modeling of the non-thermal pressure support may be difficult, it can be constrained by comparisons of the hydrostatic mass estimates with those derived from gravitational lensing for the same objects. An important caveat is that lensing measures the mass in the projected aperture while the mass within the sphere of the same radius is rather uncertain because of projection effects. Metzler et al. (2001) estimate that  $M_{500c}$  cannot be determined from weak lensing with better than  $\pm 30\%$  uncertainty. Any comparisons of X-ray hydrostatic and weak lensing masses must be done in an average sense, e.g. through derived normalizations of the correlation between the  $M_{\text{tot}}$  and a low-scatter mass proxy such as  $Y_X$  (Kravtsov et al. 2006b) or  $T_{\text{spec}}$ .

To summarize, our results indicate that an X-ray analysis of relaxed clusters correctly recovers gas density and *thermal electron* pressure gradients. The simulations provide an upper limit (5%–20% depending on radius) for the mass bias due to turbulent motions. The contribution of other pressure components will have to be constrained by future observations.

### 5.3. Implications for Cluster-Based Cosmological Tests

#### 5.3.1. Tests Based on $f_{\text{gas}}$

X-ray measurements of the baryonic mass fraction in massive clusters can be used to constrain  $\Omega_M$  or  $h$  (White et al. 1993) and also provide a potential standard candle (Sasaki 1996; Pen 1997; Allen et al. 2004). The major observational

ingredient in these tests is a measurement of the hot gas mass fraction within a sufficiently large radius. Our analysis provides clues for biases in  $f_{\text{gas}}$  measurements from high-quality *Chandra* data. We find that the  $f_{\text{gas}}$  determinations are biased high, primarily because the hydrostatic method underestimates the total cluster mass. As was discussed above, the bias in the hydrostatic estimates is related to the physical processes in the ICM (e.g., turbulence, cosmic ray and magnetic pressures etc.) and not to the deficiencies of the X-ray analysis. Further progress in confirming validity of  $f_{\text{gas}}$  measurements will have to rely on independent determinations of cluster total mass (see discussion in § 5.2). Some sources of the bias (e.g., turbulence) could be minimized if we focus only on relaxed systems. We find that in such systems, both bias and scatter in  $f_{\text{gas}}$  can be controlled to within about 5%–8% at  $r_{2500c}$  and 15%–20% at  $r_{500c}$ , which can be considered the upper limits on the  $f_{\text{gas}}$  measurement bias caused by turbulence (see § 5.2).

Note that if the ICM turbulence and other processes discussed in § 5.2 do play a role in biasing the hydrostatic mass estimates, the bias can potentially be redshift-dependent since the merger rate increases at higher  $z$  (e.g. Gottlöber et al. 2001). We do not find any detectable redshift dependence of the bias in the  $f_{\text{gas}}$  measurements in relaxed systems. However, our upper limits,  $\sim 5\%$ , are weaker than the accuracy required, e.g., for using  $f_{\text{gas}}$  as a standard ruler in the dark energy studies (Allen et al. 2004). Mock analysis of much larger cluster samples will be required to properly address this issue.

#### 5.3.2. Tests Based on the Cluster Mass Function

Another group of cosmological tests are those based on measurements of the cluster mass function. The relevant issue for our work is how well various mass proxies can be measured. A related question is how well the cluster mass vs. proxy relation can be calibrated by the X-ray analysis, which was discussed in § 5.2.

We did not discuss the easiest X-ray mass proxy, the total luminosity, because it is also the least accurate and least reliably reproduced by numerical simulations. The next, in terms of being easily measured, is the average ICM temperature. The practical averages to use are  $T_{\text{spec}}$  or  $T_{\text{spec}}[0.5r_{500c}]^8$ . These definitions are freely interchangeable since the ratio  $T_{\text{spec}}[0.5r_{500c}]/T_{\text{spec}}$  is nearly the same in all clusters (Fig.6, Table 3). One disadvantage of the spectral temperature as a mass proxy is that its measurement is somewhat sensitive to the cluster dynamical state and small-scale substructure. This sensitivity arises because  $T_{\text{spec}}$  is rather sensitive to the presence of lower-temperature components. This effect contributes to the systematic difference in the normalizations of the  $M - T$  relation between relaxed and non-relaxed clusters and also slight deviations from the self-similar evolution (Table 4). Some implications of this effect for the cosmological measurements are discussed by Rasia et al. (2005). The prospects for calibrating the  $T_{\text{spec}}$  measurement biases by cosmological numerical simulations are mixed. The effects related to the cluster dynamics, such as merger activity and shocks etc., are treated sufficiently accurately. However, the biases caused by the presence of undetected cold clumps will require a more realistic modeling of the ICM cooling and associated feedback.

More accurate X-ray proxies for cluster total mass is the

<sup>8</sup> Other definitions such as  $T_{\text{mg}}$  require measurements of the temperature profiles which is feasible only for a few best-observed clusters.

mass of the hot gas,  $M_{\text{gas}}$ , and the “X-ray  $Y$ -parameter”,  $Y_X = M_{\text{gas}} \times T_{\text{spec}}$  (Kravtsov et al. 2006b). The properties of  $Y_X$  (this is the best X-ray mass proxy known) are extensively discussed elsewhere (Kravtsov et al. 2006b), so we concentrate on  $M_{\text{gas}}$  here. The  $M_{\text{gas}}$  is measured very reliably. The average bias is  $< 5\%$  with only a few strong outliers (Fig.4) and there is no detectable redshift dependence. A similar accuracy should in principle be achieved for the  $M_{\text{tot}}$  estimates since to the first order,  $M_{\text{tot}} \propto M_{\text{gas}}$ . Note that the biases in  $M_{\text{gas}}$  measurements are mostly due to large-scale deviations of the cluster body from spherical symmetry. This effect should be reliably treated in the current generation cosmological simulations, and so the accuracy of the  $M_{\text{gas}}$ -based total mass estimates can be improved yet further. All we need is a larger sample of simulated clusters. A major obstacle, however, is the uncertainties in the mass fraction of cold baryons (stars and molecular gas). This fraction can be substantial, as indicated by our simulations (Kravtsov et al. 2005) and significant deviations of the observed  $f_{\text{gas}}$  in clusters from the cosmic mean (e.g., Ettori 2003; Vikhlinin et al. 2006). Further progress in this area requires significant improvements in the reliability of the stellar mass measurements and treatment of the star formation in the simulations. We will further discuss these issues in the forthcoming papers.

To briefly summarize our results, we find that the analysis of deep X-ray observations of galaxy clusters can reliably

recover its intended targets: the distribution of density and temperature of the hot ICM. The accuracy of estimating the total cluster mass from these parameters is limited by additional physical processes in the ICM, such as turbulence, magnetic and cosmic ray pressure, and possible departures from the electron-ion equilibrium. Our work provides a realistic estimate of the effects of turbulence, which are found to cause underestimation of  $M_{\text{tot}}$  by 5%–20% in clusters that can be visually classified as relaxed (this can be considered as an upper limit for the bias if the ICM viscosity is non-negligible). Constraining the role of other effects will probably have to rely on accurate independent mass measurements (e.g., by weak lensing) in a large, complete cluster sample.

We thank Elena Rasia for a careful reading of this manuscript. DN is supported by the Sherman Fairchild Postdoctoral Fellowship at Caltech. AV is supported by the NASA grant NAG5-9217 and contract NAS8-39073. AVK is supported by the National Science Foundation (NSF) under grants No. AST-0239759 and AST-0507666, by NASA through grant NAG5-13274, and by the Kavli Institute for Cosmological Physics at the University of Chicago. The cosmological simulations used in this study were performed on the IBM RS/6000 SP4 system (copper) at the National Center for Supercomputing Applications (NCSA).

## REFERENCES

- Allen, S. W., Schmidt, R. W., Ebeling, H., Fabian, A. C., & van Speybroeck, L. 2004, *MNRAS*, 353, 457
- Anders, E. & Grevesse, N. 1989, *Geochim. Cosmochim. Acta*, 53, 197
- Bryan, G. L. & Norman, M. L. 1998, *ApJ*, 495, 80
- Cavaliere, A. & Fusco-Femiano, R. 1978, *A&A*, 70, 677
- Dolag, K., Vazza, F., Brunetti, G., & Tormen, G. 2005, *MNRAS*, 364, 753
- Ettori, S. 2003, *MNRAS*, 344, L13
- Ettori, S., De Grandi, S., & Molendi, S. 2002, *A&A*, 391, 841
- Evrard, A. E., Metzler, C. A., & Navarro, J. F. 1996, *ApJ*, 469, 494
- Faltenbacher, A., Kravtsov, A. V., Nagai, D., & Gottlöber, S. 2005, *MNRAS*, 358, 139
- Ferland, G. J., Korista, K. T., Verner, D. A., Ferguson, J. W., Kingdon, J. B., & Verner, E. M. 1998, *PASP*, 110, 761
- Fox, D. C. & Loeb, A. 1997, *ApJ*, 491, 459
- Frenk, C. S., et al. 1999, *ApJ*, 525, 554
- Gottlöber, S., Klypin, A., & Kravtsov, A. V. 2001, *ApJ*, 546, 223
- Haardt, F. & Madau, P. 1996, *ApJ*, 461, 20
- Inogamov, N. A. & Sunyaev, R. A. 2003, *Astronomy Letters*, 29, 791
- Kaastra, J. S. & Mewe, R. 1993, *A&AS*, 97, 443
- Kennicutt, R. C. 1998, *ApJ*, 498, 541
- Klypin, A., Kravtsov, A. V., Bullock, J. S., & Primack, J. R. 2001, *ApJ*, 554, 903
- Kotov, O. & Vikhlinin, A. 2006, *ApJ*, 641, 752
- Kravtsov, A. V. 1999, High-resolution simulations of structure formation in the Universe, Ph.D. thesis, New Mexico State University
- Kravtsov, A. V., Klypin, A., & Hoffman, Y. 2002, *ApJ*, 571, 563
- Kravtsov, A. V., Nagai, D., & Vikhlinin, A. A. 2005, *ApJ*, 625, 588
- Kravtsov, A. V., Nagai, D., & Vikhlinin, A. A. 2006a, *ApJ*, in preparation
- Kravtsov, A. V., Vikhlinin, A. A., & Nagai, D. 2006b, *ApJ*, in press (astro-ph/0603205)
- Lau, E., Kravtsov, A. V., & Nagai, D. 2006, *ApJ*, in preparation
- Liedahl, D. A., Osterheld, A. L., & Goldstein, W. H. 1995, *ApJ*, 438, L115
- Markevitch, M. 2005, astro-ph/0511345
- Markevitch, M., Mushotzky, R., Inoue, H., Yamashita, K., Furuzawa, A., & Tawara, Y. 1996, *ApJ*, 456, 437
- Markevitch, M., et al. 2003, *ApJ*, 583, 70
- Mathiesen, B., Evrard, A. E., & Mohr, J. J. 1999, *ApJ*, 520, L21
- Mathiesen, B. F. & Evrard, A. E. 2001, *ApJ*, 546, 100
- Mazzotta, P., Rasia, E., Moscardini, L., & Tormen, G. 2004, *MNRAS*, 354, 10
- Metzler, C. A., White, M., & Loken, C. 2001, *ApJ*, 547, 560
- Mewe, R., Gronenschild, E. H. B. M., & van den Oord, G. H. J. 1985, *A&AS*, 62, 197
- Muanwong, O., Thomas, P. A., Kay, S. T., Pearce, F. R., & Couchman, H. M. P. 2001, *ApJ*, 552, L27
- Nagai, D., Kravtsov, A. V., & Vikhlinin, A. A. 2006, *ApJ*, in preparation
- Pen, U. 1997, *New Astronomy*, 2, 309
- Rasia, E., Mazzotta, P., Borgani, S., Moscardini, L., Dolag, K., Tormen, G., Diaferio, A., & Murante, G. 2005, *ApJ*, 618, L1
- Rasia, E., et al. 2006, *MNRAS*, 369, 2013
- Ruszkowski, M., Brüggem, M., & Begelman, M. C. 2004a, *ApJ*, 611, 158
- Ruszkowski, M., Brüggem, M., & Begelman, M. C. 2004b, *ApJ*, 615, 675
- Sasaki, S. 1996, *PASJ*, 48, L119
- Schuecker, P., Finoguenov, A., Miniati, F., Böhringer, H., & Briel, U. G. 2004, *A&A*, 426, 387
- Sijacki, D. & Springel, V. 2006, submitted to *MNRAS* (astro-ph/0605301)
- Springel, V. 2005, *MNRAS*, 364, 1105
- Vikhlinin, A. 2006, *ApJ*, 640, 710
- Vikhlinin, A., Kravtsov, A., Forman, W., Jones, C., Markevitch, M., Murray, S. S., & V., S. L. 2006, *ApJ*, 640, 691
- Vikhlinin, A., Markevitch, M., Murray, S. S., Jones, C., Forman, W., & Van Speybroeck, L. 2005, *ApJ*, 628, 655
- Vikhlinin, A., McNamara, B. R., Forman, W., Jones, C., Quintana, H., & Hornstrup, A. 1998, *ApJ*, 502, 558
- White, S. D. M., Navarro, J. F., Evrard, A. E., & Frenk, C. S. 1993, *Nature*, 366, 429